Letters

Transient Synchronization Stability Analysis and Enhancement of DFIG-Based Wind Turbines From Perspective of Power Transmission Balance

Donghai Zhu, *Senior Member, IEEE*, Chencan Zheng, Yihang Yang, Jiabing Hu, *Senior Member, IEEE*, Xudong Zou, and Yong Kang, *Fellow, IEEE*

***Abstract*—During low voltage ride through, the DFIG-based wind turbine faces the risk of transient synchronization instability, due to the absence of equilibrium point. To cope with it, this letter analyzes the existence mechanism of equilibrium point from the perspective of active power transmission balance. Then, a power transmission balance control is proposed to enhance synchronization stability, which is independent of grid parameters. The proposed method can maintain synchronization stability during severe grid voltage dips and frequency deviations. Finally, the proposed method is validated by experiments.**

***Index Terms*—DFIG-based wind turbines, equilibrium point, low voltage ride through, power transmission balance, synchronization stability.**

I. Introduction

With the increasing penetration of renewable energy resources, the safety and stability of wind turbines (WTs) have received widespread attention [1]. In general, the grid codes require wind turbines to possess low voltage ride through (LVRT) capability and inject reactive current during grid faults. Synchronization stability is the prerequisite for successful LVRT [2], which requires the existence of equilibrium point [3]. If there is no equilibrium point, the output frequency of phase-locked loop (PLL) will continuously shift until it completely deviates from the power grid. This phenomenon is referred to as the loss of synchronization (LOS) [4], which will result in LVRT control failure.

Some scholars have explored the existence mechanism of equilibrium point. The common approaches involve mathematical analysis through the establishment of voltage vector relationships or quasi-steady-state equations. Pei et al. [5] used voltage vector triangle method to derive the existence boundaries of equilibrium point for WTs. Dong et al. [6] proposed a state-feedback quasi-steady-state PLL model, providing in-depth analysis for the behaviors of PLL during synchronization instability. Furthermore, the "I_d-V_t" plane based on quasi-steady-state model was adopted to investigate the existence of the equilibrium point [7]. During LVRT, constrained by grid codes, the equilibrium point is generally ensured by adjusting the active current of WTs. One class of methods is calculating errors with rated frequency, thereby modifying current commands. An active current injection method based on PLL frequency was proposed to solve the LOS problem in [8]. He et al. [9] integrated the frequency error control with the current control loop, enhancing synchronization stability by improving system damping. However, because these methods rely on additional PI controllers to generate references, complex parameter tuning is required in practical applications. Additionally, when grid voltage sag faults are accompanied by frequency deviation, these methods will even deteriorate stability. Another class of methods directly specifies the active current reference. An adaptive current injection based on the R/X ratio of grid impedance was proposed in [10]. However, this method requires accurate estimation of the grid impedance, which is difficult in engineering implementation.

In essence, when the WT operates at an equilibrium point, the system can maintain active power transmission balance. Therefore, this letter analyzes the physical mechanism of the existence of equilibrium point from the perspective of active power transmission balance. Based on this, a power transmission balance control is proposed for DFIG-based WTs to avoid LOS. The method is simple and reliable in practice since it is independent of grid parameters and avoids the introduction of additional PI controller.

II. System Description and Modeling

Fig. 1 illustrates the generic topology and control block of a DFIG-based WT connected to weak grid. The WT is integrated into the grid U_g through a step-up transformer and transmission line, which is represented by the grid impedance Z_g. When the grid fault is detected, the WT is taken over by LVRT control.

Received 18 April 2025; revised 10 June 2025 and 3 July 2025; accepted 23 July 2025. Date of publication 29 July 2025; date of current version 22 October 2025. This work was supported in part by the National Natural Science Fund for Distinguished Young Scholars of China under Grant 52225704 and in part by the Natural Science Foundation of Hubei Province under Grant 2025AFA102. *(Corresponding author: Jiabing Hu.)*

Donghai Zhu, Chencan Zheng, Jiabing Hu, Xudong Zou, and Yong Kang are with the State Key Laboratory of Advanced Electromagnetic Technology, School of Electrical and Electronic Engineering, Huazhong University of Science and Technology, Wuhan 430074, China (e-mail: zhudh@hust.edu.cn; m202372270@hust.edu.cn; j.hu@mail.hust.edu.cn; xdzou@mail.hust.edu.cn; ykang@hust.edu.cn).

Yihang Yang is with the China Electric Power Planning and Engineering Institute, Beijing 100120, China (e-mail: yhyang@eppei.com).

Color versions of one or more figures in this article are available at https://doi.org/10.1109/TPEL.2025.3593482.

Digital Object Identifier 10.1109/TPEL.2025.3593482

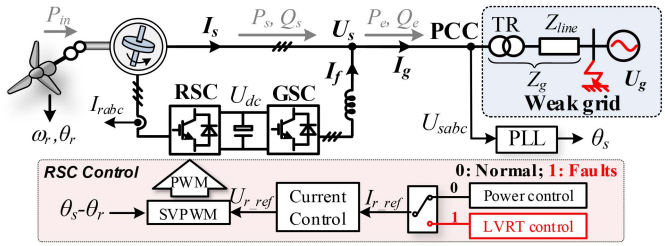

Fig. 1. Generic topology and control block of DFIG-based WT in weak grid.

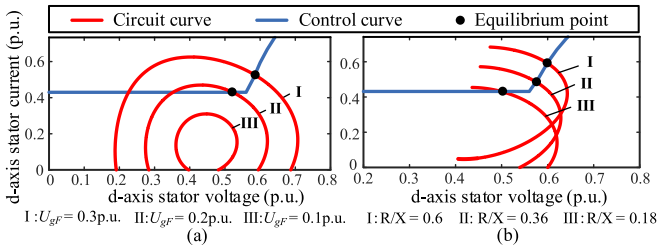

Fig. 2. "U_s-I_{sd}" plane under MAC injection method. (a) With different U_{gF}. (b) With different R/X ratios.

The stator and rotor vectors adopt generator and motor convention, respectively. Neglecting the flux dynamic and stator resistance R_s, the stator voltage can be expressed as [11]

$$\begin{cases} U_{sd} = -\omega_s L_m I_{rq} + \omega_s L_s I_{sq} = -X_m I_{rq} + X_s I_{sq} \\ U_{sq} = \omega_s L_m I_{rd} - \omega_s L_s I_{sd} = X_m I_{rd} - X_s I_{sd} \end{cases} \tag{1}$$

where L_m is the magnetizing inductance and L_s is the stator inductance, respectively. ω_s is the stator angular frequency, $X_m = \omega_s L_m$ and $X_s = \omega_s L_s$. ψ_s, U_s, I_s, and I_r are stator flux, stator voltage, stator current, and rotor current, respectively. Subscripts "d" and "q" denote the d- and q-axis components.

Based on the grid voltage vector $\boldsymbol{U}_g$ as reference, the angle between stator voltage vector $\boldsymbol{U}_s$ and $\boldsymbol{U}_g$ is defined as power angle δ. The external network quasi-static equation in weak grid can be described as follows during fault:

$$\begin{cases} U_{sd} = U_{gF}\cos\delta + R_g I_{gd} - X_g I_{gq} \\ U_{sq} = -U_{gF}\sin\delta + R_g I_{gq} + X_g I_{gd} \end{cases} \tag{2}$$

where R_g and X_g are grid resistance and reactance. U_{gF} is grid voltage during fault. The d- and q-axis component of injected current vector $\boldsymbol{I}_g$ at PCC can be expressed as

$$\begin{cases} I_{gd} = (1-s) I_{sd} \\ I_{gq} = I_{sq} \end{cases} \tag{3}$$

where s is the slip rate of DFIG-based WT.

III. Synchronization Instability Issues

During LVRT, the DFIG-based WTs need to inject a certain amount of reactive current into the power system to support the grid, and the rotor current can be expressed as [12]

$$I_{rq} = -K_q \times (0.9 - U_s), 0.2 \le U_s \le 0.9 \tag{4}$$

where the reactive current ratio coefficient K_q ranges from 1.5 to 3 [12], and the maximum value of I_{rq} is set to 1 p.u.

Regarding the active current I_{rd}, there are two typical injection methods: the maximum active current (MAC) injection method and zero active current (ZAC) injection method. The synchronization instability phenomena and influencing factors under two typical injection methods will be analyzed below.

A. Maximum Active Current Injection Method

The rotor active current reference of MAC injection method can be expressed as

$$I_{rd} = \sqrt{I_{r\max}^2 - I_{rq}^2} \tag{5}$$

where $I_{r\max}$ is the maximum capacity of RSC, taken as 1.1 p.u.

If the equilibrium point exists, the basic steady-state condition $U_{sq} = 0$ for voltage vector orientation control should be satisfied. When the MAC injection method is adopted, combining (1), (2), (5) with $U_{sq} = 0$, the relation between I_{sd} and U_{sd} can be obtained from the perspective of external circuit

$$\begin{aligned} &\left[U_{sd} + X_g\left(U_{sd} - \sqrt{X_m^2 I_{r\max}^2 - X_s^2 I_{sd}^2}\right)\right. \\ &\left./X_s - R_g(1-s)I_{sd}\right]^2 \\ &+\left[R_g\left(U_{sd} - \sqrt{X_m^2 I_{r\max}^2 - X_s^2 I_{sd}^2}\right)/X_s + X_g(1-s)I_{sd}\right]^2 \\ &= U_{gF}^2. \end{aligned} \tag{6}$$

Meanwhile, combining (1), (4), (5) with $U_{sq} = 0$, the relation between I_{sd} and U_{sd} under LVRT control is obtained as

$$I_{sd} = \frac{X_m}{X_s} I_{rd} = \frac{X_m}{X_s}\sqrt{I_{r\max}^2 - K_q^2 (0.9 - U_{sd})^2}. \tag{7}$$

Fig. 2 illustrates the "U_s-I_{sd}" plane under MAC injection method. The red line derived from (6) represents circuit curve, and the blue line derived from (7) represents the control curve. The intersection point between two curves represents the equilibrium point. In Fig. 2(a), as U_{gF} decreases, the circuit curve gradually becomes smaller. When there is no intersection point, the equilibrium point of the system will be lost. In Fig. 2(b), as the ratio of grid resistance to inductance (R/X) decreases, the circuit curve is shifted downwards and the equilibrium point tends to be lost.

B. ZAC Injection Method

Under ZAC injection method, the rotor active current reference can be expressed as

$$I_{rd} = 0. \tag{8}$$

Based on (1), (2), (8), with $U_{sq} = 0$, the following equation can be obtained from the perspective of external circuit:

$$\begin{aligned} &\left[U_{sd} + X_g\left(U_{sd} + X_m I_{rq}\right)/X_s - R_g(1-s)I_{sd}\right]^2 \\ &+\left[R_g\left(U_{sd} + X_m I_{rq}\right)/X_s + X_g(1-s)I_{sd}\right]^2 = U_{gF}^2. \end{aligned} \tag{9}$$

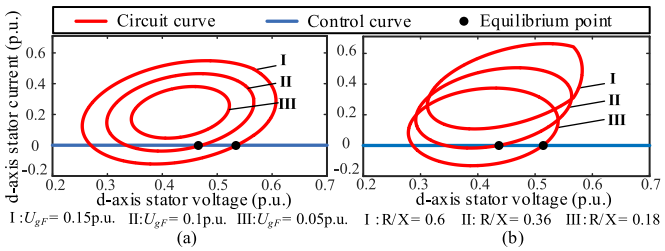

Fig. 3. "U_s-I_{sd}" plane under ZAC injection method. (a) With different U_{gF}. (b) With different R/X.

Combining (1), (4), (8) with $U_{sq} = 0$, I_{sd} under LVRT control can be expressed as

$$I_{sd} = X_m I_{rd}/X_s = 0. \tag{10}$$

Fig. 3 illustrates the "U_s-I_{sd}" plane under ZAC injection method. The red line is derived from (9) and the blue line is derived from (10). In Fig. 3(a), as U_{gF} decreases, the circuit curve gradually becomes smaller. In Fig. 3(b), as R/X increases, the circuit curve is shifted upwards. The above two cases will lead to the intersection point being lost.

In summary, both typical current injection methods will lead to the absence of equilibrium point when U_g deeply drops or R/X is inappropriate. The decrease of U_{gF} will reduce the power transmission capacity of system, while R/X reflects the active power consumed by the line impedance. Both factors affecting the existence of the equilibrium point are closely related to active power transmission. Therefore, the physical mechanisms for the existence of equilibrium point can be further explored from the perspective of active power transmission balance.

IV. Synchronization Instability Mechanism

A. Vector Relationship Under Transmission Power Balance

According to Fig. 1, the output active power of WT at the PCC point is P_e, the active power transmitted at the grid voltage U_g is P_g, and the active power loss on the grid impedance Z_g is P_{loss}. The active power balance can be expressed as

$$P_e = I_g U_s \cos\theta_i = \underbrace{I_g U_{gF} \cos(\theta_i - \delta)}_{P_g} + \underbrace{I_g^2 R_g}_{P_{\text{loss}}} \tag{11}$$

where θ_i represents the phase angle between vector $\boldsymbol{U}_s$ and $\boldsymbol{I}_g$. The active power loss P_{loss} can be further expressed as

$$P_{\text{loss}} = I_g^2 R_g = I_g^2 Z_g \cos\theta_z = I_g U_{vf} \cos\theta_z \tag{12}$$

where U_{vf} denotes the voltage drop across the grid impedance and θ_z represents the grid impedance phase angle. Combining (11) with (12), the following expression is obtained:

$$U_s \cos\theta_i = U_{gF} \cos(\theta_i - \delta) + U_{vf} \cos\theta_z \tag{13}$$

where $U_s\cos\theta_i$, $U_{vf}\cos\theta_z$, and $U_{gF}\cos(\theta_i - \delta)$ correspond to P_e, P_{loss}, and P_g, respectively, which denote the projections of the stator voltage vector, the grid impedance voltage vector, and the grid voltage vector in the direction of $\boldsymbol{I}_g$. Equation (13) converts the power balance relationship (12) into a voltage scalar relationship in the direction of $\boldsymbol{I}_g$, as the red line shown in Fig. 4(a).

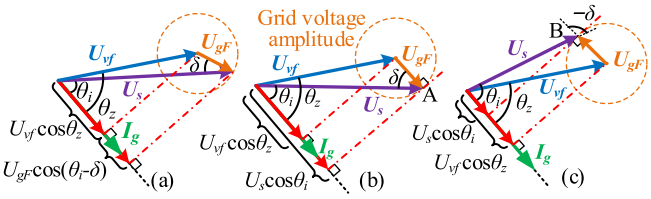

Fig. 4. Vector relationship characterizing the power balance. (a) General case. (b) Maximum active power output. (c) Minimum active power output.

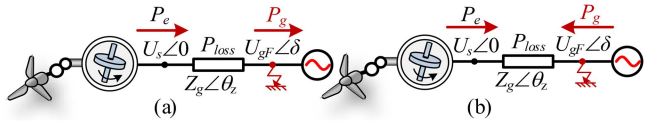

Fig. 5. Power flow direction. (a) Maximum active power output. (b) Minimum active power output.

The vector relationship shown in Fig. 4 can further illustrate the active power transmission limit of the system and physical mechanism of equilibrium point absence caused by active power exceeding the limit.

B. Absence Mechanism of Equilibrium Point

Fig. 4(b) illustrates the maximum value of $U_s\cos\theta_i$. The red dotted line perpendicular to $\boldsymbol{I}_g$ is tangent to the grid voltage amplitude circle at the point A, which is the end point of the stator voltage vector $\boldsymbol{U}_s$. The corresponding P_e is the maximum value. Additionally, since the grid voltage vector $\boldsymbol{U}_{gF}$ is parallel and in the same direction as $\boldsymbol{I}_g$, there is $\theta_i = \delta$, and P_g also reaches its maximum value, which can be expressed as

$$P_{g\max} = I_g U_{gF}. \tag{14}$$

Fig. 5(a) illustrates the power flow direction when DFIG outputs the maximum active power. The P_e is consumed by the line impedance and the remained active power is transmitted to the grid. When P_e reaches the maximum output active power limit, the power imbalance will be triggered and the system will lose equilibrium point, i.e.,

$$P_e > P_{g\max} + P_{\text{loss}}. \tag{15}$$

Fig. 4(c) illustrates the minimum value of $U_s\cos\theta_i$. The red dotted line perpendicular to $\boldsymbol{I}_g$ is tangent to the grid voltage amplitude circle at the point B, which is the end point of $\boldsymbol{U}_s$. The corresponding P_e is the minimum value. Since $\boldsymbol{U}_{gF}$ is parallel and in the opposite direction as $\boldsymbol{I}_g$, P_g is minimized. Then, there is $\theta_i - \delta = 180°$, and P_g can be expressed as

$$P_{g\min} = -I_g U_{gF}. \tag{16}$$

Fig. 5(b) illustrates the power flow direction when DFIG outputs the minimum active power. When P_e is too small, P_e and the power absorbed from the grid P_g are combined to satisfy the P_{loss}. When P_e reaches the minimum output active power

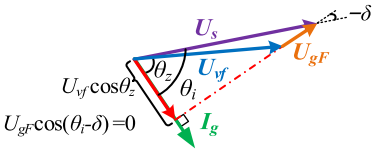

Fig. 6. Voltage vector relationship under power transmission balance control.

limit, the power imbalance will be triggered, i.e.,

$$P_e < P_{\text{loss}} + P_{g\min}. \tag{17}$$

In conclusion, the physical essence of equilibrium point absence is that the output active power reference of wind turbine exceeds the transmission capacity of system. The MAC and ZAC injection methods correspond to the cases that the active power reference is excessively high and low, respectively.

V. Power Transmission Balance Control

A. Principle and Implementation Method

According to the above analysis, it can be inferred that if P_e fully compensates P_{loss}, that is $P_g = 0$, the active power transmission will remain balanced, as shown in Fig. 6. This situation is most conducive to the existence of equilibrium point. Based on this idea, this letter proposes a power transmission balance control for DFIG-based WTs to enhance synchronization stability.

Regardless of the grid conditions, when the $\boldsymbol{I}_g$ is orthogonal to $\boldsymbol{U}_{gF}$, the geometric relationship between vectors determines that P_g will be adaptively adjusted to zero. Therefore, the I_{gd} should be regulated as

$$I_{gd} = I_{gq}/\cot\delta. \tag{18}$$

Combining (1), (3), (4) with (18), the rotor active current reference under the proposed method can be derived as

$$I_{rd\_ref} = \frac{(X_m K_q + 1)U_{sd} - 0.9X_m K_q}{X_m(1-s)\cot\delta}, K_q(0.9 - U_s) \le 1 \tag{19}$$

where the power angle δ can be calculated from PLL, i.e.,

$$\delta = \int_{0\text{ms}}^{100\text{ms}} (\omega_{\text{pll}} - \omega_N) \tag{20}$$

where ω_{pll} is angular frequency of PLL. ω_N is the rated angular frequency. The dynamic response timescale of PLL is approximately from a few tens to 100 ms [13]. Therefore, the proposed method only performs integration within 100 ms after fault occurs, which can avoid the continuous error caused by the deviation of grid frequency ω_g from ω_N. Fig. 7 shows the control block of the proposed method.

In contrast to the injection method based on PLL frequency [8], the reference of the proposed control method is directly obtained from algebraic operations, without the requirement of PI controller to output the reference. Furthermore, the proposed control method is independent of grid parameters, distinguishing it from the R/X method [10]. Therefore, the method is simpler and more reliable in practice.

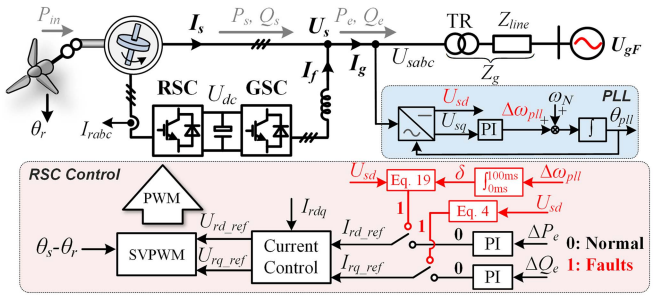

Fig. 7. Control block of proposed method.

The proposed method is oriented to the fault duration stage. After the existing LVRT control strategies suppress the overcurrent at the fault occurrence stage, the rotor current reference will be given by the proposed method. Therefore, the proposed method can be naturally integrated with existing LVRT control strategies.

B. Quantitative Analysis of Stability Margin

The stability margin can be further analyzed quantitatively.

If I_{rd} reaches the maximum limit $I_{rd\cdot\max}$ that maintains the existence of equilibrium point, there is $\theta_i = \delta$. Combining (1), (2), (3), $\theta_i = \delta$ with $U_{sq} = 0$, the following equations can be obtained:

$$\begin{cases} U_{sd} = \dfrac{U_{gF}(1-s)X_m I_{rd\_\max}}{\sqrt[2]{[(1-s)X_m I_{rd\_\max}]^2 + (U_{sd}-X_m)^2}} \\ \qquad + R_g(1-s)\dfrac{X_m}{X_s} I_{rd\_\max} - X_g \dfrac{U_{sd}-X_m}{X_s} \\ 0 = \dfrac{U_{gF}(U_{sd}-X_m)}{\sqrt[2]{[(1-s)X_m I_{rd\_\max}]^2 + (U_{sd}-X_m)^2}} \\ \qquad + R_g \dfrac{U_{sd}-X_m}{X_s} + X_g(1-s)\dfrac{X_m}{X_s} I_{rd\_\max}. \end{cases} \tag{21}$$

The two equations of (21) involve three variables: $I_{rd\cdot\max}$, U_{sd}, and U_{gF}. By simultaneously solving the two equations, U_{sd} can be eliminated. The $I_{rd\cdot\max}$ under different U_{gF} can be obtained.

Similarly, If I_{rd} reaches the minimum $I_{rd\cdot\min}$ limit that maintains the existence of equilibrium point, there is $\theta_i - \delta = 180°$. Combining (1), (2), (3), $\theta_i - \delta = 180°$ with $U_{sq} = 0$, the following equations can be obtained:

$$\begin{cases} U_{sd} = \dfrac{-U_{gF}(1-s)X_m I_{rd\_\min}}{\sqrt[2]{[(1-s)X_m I_{rd\_\min}]^2 + (U_{sd}-X_m)^2}} \\ \qquad + R_g(1-s)\dfrac{X_m}{X_s} I_{rd\_\min} - X_g \dfrac{U_{sd}-X_m}{X_s} \\ 0 = \dfrac{-U_{gF}(U_{sd}-X_m)}{\sqrt[2]{[(1-s)X_m I_{rd\_\min}]^2 + (U_{sd}-X_m)^2}} \\ \qquad + R_g \dfrac{U_{sd}-X_m}{X_s} + X_g(1-s)\dfrac{X_m}{X_s} I_{rd\_\min}. \end{cases} \tag{22}$$

The two equations of (22) also involve three variables: $I_{rd\cdot\min}$, U_{sd}, and U_{gF}. By simultaneously solving the two equations, the $I_{rd\cdot\min}$ under different U_{gF} can be obtained.

Furthermore, the stability margin metric k can be defined based on the rotor active current boundary $I_{rd\cdot\max}$ and $I_{rd\cdot\min}$

$$k = \min\{I_{rd} - I_{rd\_\min}, I_{rd\_\max} - I_{rd}\} \tag{23}$$

TABLE I
PARAMETERS OF 1.5-MW DFIG-BASED WT SYSTEM

Parameter	Value	Parameter	Value
Rated power	1.5 MW	Rated stator voltage	690 V
Pairs of poles	2	Rated DC-bus voltage	1200 V
Rated frequency	50 Hz	Mutual inductance	2.9 p.u.
Rotor resistance	0.016 p.u.	Rotor leakage inductance	0.16 p.u.
Stator resistance	0.023 p.u.	Stator leakage inductance	0.18 p.u.

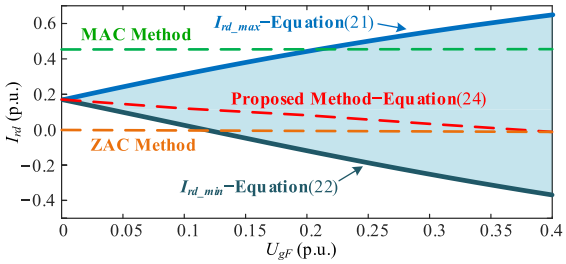

Fig. 8. I_{rd}–U_{gF} curves of different methods and system's stability boundary.

TABLE II
STABILITY MARGIN UNDER DIFFERENT INJECTION METHODS

Method \ U_{gF}	0.05p.u.	0.10p.u.	0.15p.u.	0.20p.u.
MAC method	$k=-0.21$	$k=-0.14$	$k=-0.06$	$k=0.01$
ZAC method	$k=-0.11$	$k=-0.04$	$k=0.03$	$k=0.11$
Proposed method	$k=0.05$	$k=0.10$	$k=0.16$	$k=0.21$

where k represents the minimum difference between the actual rotor active current I_{rd} and the stability boundary. A larger value of k indicates that I_{rd} is located deeper within the stable boundary and the system's stability margin is higher. If $k<0$, it indicates that I_{rd} exceeds the system's transmission capacity and no equilibrium point exists.

When adopting proposed method, the relationship equation of I_{rd} and U_{gF} is determined by combining (1), (2), (3), (19)

$$\begin{cases} U_{sd} = U_{gF}\cos\delta + R_g(1-s)\frac{X_m}{X_s}I_{rd} - X_g\frac{U_{sd}-X_m}{X_s} \\ 0 = -U_{gF}\sin\delta + R_g\frac{U_{sd}-X_m}{X_s} + X_g(1-s)\frac{X_m}{X_s}I_{rd} \\ \delta = \operatorname{arccot}\frac{U_{sd}-X_m}{(1-s)X_m I_{rd}}. \end{cases} \quad (24)$$

For the DFIG-based WT with parameters given in Table I, the relationship curves between I_{rd} and U_{gF} under different injection methods can be drawn, as shown in Fig. 8. Based on this, the stability margins under specified fault depths can be obtained, as shown in Table II. It can be seen that the proposed method exhibits better stability margin under deep faults.

VI. EXPERIMENTAL VERIFICATION

To validate the proposed method, a hardware-in-the-loop (HIL) experimental setup is constructed [14], as shown in Fig. 9. The SpaceR system is an electromagnetic transient simulation software offering interfaces to the control system. The main circuit topology of WT shown in Fig. 1 is simulated by the SpaceR. The wind farm adopts aggregation model containing 50 DFIG-based WTs. The system parameters are given in Table I.

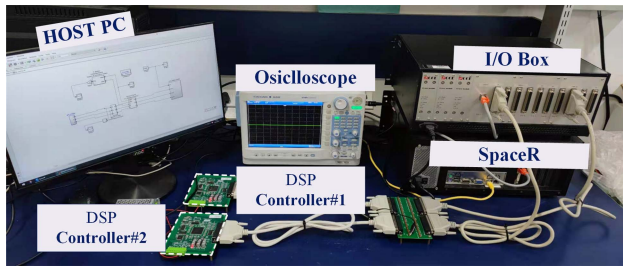

Fig. 9. Photo of the HIL experimental setup.

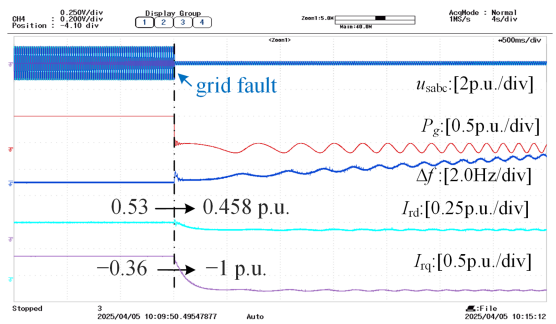

Fig. 10. Experimental results under MAC injection method.

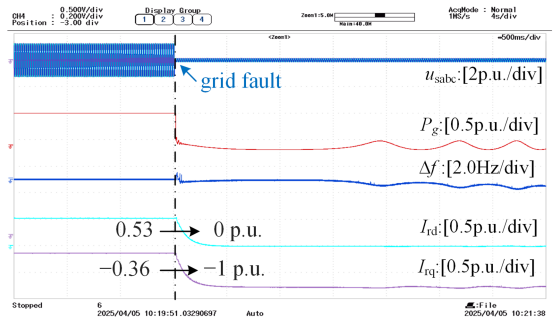

Fig. 11. Experimental results under ZAC injection method.

In the experiment, the symmetrical fault occurs in the power grid and U_g drops from 1.0 p.u. to 0.1 p.u. at 4 s. I_{rq} is set to −1 p.u. according to grid code.

Figs. 10 and 11 illustrate the LOS phenomena under two current injection methods. Under MAC and ZAC injection methods, the rotor active current references are set to 0.458 p.u. and 0 p.u., respectively. The PLL output frequency f exhibits continuous increase and decrease, respectively. This trend of increase or decrease is related to the line impedance angle and active power output during fault, which is explained in [6]. And the waveforms of P_g, I_{rd}, and I_{rq} exhibit low-frequency oscillation phenomena, causing the DFIG-based WT to lose synchronization with the grid.

Fig. 12 shows the experimental results under proposed method. When the grid fault occurs, the active rotor current is adaptively adjusted to 0.112 p.u. The PLL can keep synchronous with the power grid. Moreover, the P_g is controlled to zero, which

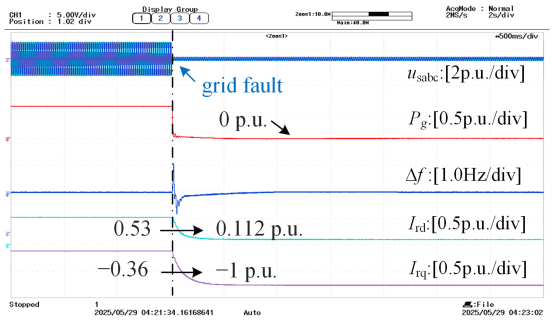

Fig. 12. Experimental results under proposed method.

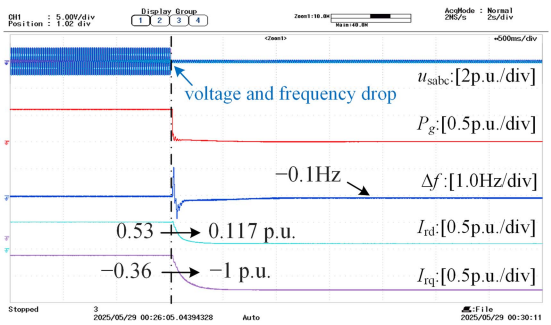

Fig. 13. Experimental results under grid frequency deviation condition.

indicates that no active power is transmitted to the grid, thereby ensuring the existence of equilibrium point.

In order to illustrate the adaptability of the proposed method under frequency deviation, the following experiment is further supplemented: The voltage amplitude U_g drops from 1.0 p.u. to 0.1 p.u. at 4 s, while ω_g decreases from 50 Hz to 49.9 Hz at 4 s.

As shown in Fig. 13, I_{rd} is adjusted to 0.117 p.u. during frequency deviation. If no frequency deviation occurs, I_{rd} will be controlled to 0.112 p.u. as Fig. 12. Therefore, the variation of I_{rd} remains within an acceptable range. No instability phenomenon is observed during the entire process. These experimental results validate the effectiveness of proposed method under grid frequency deviation condition.

VII. Conclusion

In this letter, the transient synchronization stability mechanism of DFIG-based WT is revealed from the perspective of active power transmission. It is concluded that transmitting zero power to the grid during LVRT is most conducive to ensuring the existence of equilibrium point. Based on this, a power transmission balance control independent of grid information is proposed. The experiments validate that the proposed method has good robustness against the deep grid voltage dips and grid frequency deviations.

References

[1] N. Baeckeland, D. Chatterjee, M. Lu, B. Johnson, and G.-S. Seo, "Overcurrent limiting in grid-forming inverters: A comprehensive review and discussion," *IEEE Trans. Power Electron.*, vol. 39, no. 11, pp. 14493–14517, Nov. 2024.

[2] M. G. Taul, X. Wang, P. Davari, and F. Blaabjerg, "An overview of assessment methods for synchronization stability of grid-connected converters under severe symmetrical grid faults," *IEEE Trans. Power Electron.*, vol. 34, no. 10, pp. 9655–9670, Oct. 2019.

[3] Y. Liu et al., "Transient stability enhancement control strategy based on improved PLL for grid connected VSC during severe grid fault," *IEEE Trans. Energy Convers.*, vol. 36, no. 1, pp. 218–229, Mar. 2021.

[4] Ö. Göksu, R. Teodorescu, C. L. Bak, F. Iov, and P. C. Kjær, "Instability of wind turbine converters during current injection to low voltage grid faults and PLL frequency based stability solution," *IEEE Trans. Power Syst.*, vol. 29, no. 4, pp. 1683–1691, Jul. 2014.

[5] J. Pei et al., "Characteristic analysis and risk assessment for voltage–frequency coupled transient instability of large-scale grid-connected renewable energy plants during LVRT," *IEEE Trans. Ind. Electron.*, vol. 67, no. 7, pp. 5515–5530, Jul. 2020.

[6] D. Dong, B. Wen, D. Boroyevich, P. Mattavelli, and Y. Xue, "Analysis of phase-locked loop low-frequency stability in three-phase grid-connected power converters considering impedance interactions," *IEEE Trans. Ind. Electron.*, vol. 62, no. 1, pp. 310–321, Jan. 2015.

[7] H. Yuan, H. Xin, L. Huang, Z. Wang, and D. Wu, "Stability analysis and enhancement of type-4 wind turbines connected to very weak grids under severe voltage sags," *IEEE Trans. Energy Convers.*, vol. 34, no. 2, pp. 838–848, Jun. 2019.

[8] H. Geng, L. Liu, and R. Li, "Synchronization and reactive current support of PMSG-based wind farm during severe grid fault," *IEEE Trans. Sustain. Energy*, vol. 9, no. 4, pp. 1596–1604, Oct. 2018.

[9] X. He, H. Geng, R. Li, and B. C. Pal, "Transient stability analysis and enhancement of renewable energy conversion system during LVRT," *IEEE Trans. Sustain. Energy*, vol. 11, no. 3, pp. 1612–1623, Jul. 2020.

[10] S. Ma, H. Geng, L. Liu, G. Yang, and B. C. Pal, "Grid-synchronization stability improvement of large scale wind farm during severe grid fault," *IEEE Trans. Power Syst.*, vol. 33, no. 1, pp. 216–226, Jan. 2018.

[11] D. Zhu, X. Zou, S. Zhou, W. Dong, Y. Kang, and J. Hu, "Feedforward current references control for DFIG-based wind turbine to improve transient control performance during grid faults," *IEEE Trans. Energy Convers.*, vol. 33, no. 2, pp. 670–681, Jun. 2018.

[12] W. S. Wang, Y. N. Chi, Y. Li, H. Tang, and J. Hu, *Technical Specification For Connecting Wind Farm to Power System—Part 1 : Onshore Wind Power, Chinese Standard: GB/T 19963.1-2021*. Beijing, China: Standards Press of China, 2021.

[13] H. Yuan, X. Yuan, and J. Hu, "Modeling of grid-connected VSCs for power system small-signal stability analysis in DC-link voltage control timescale," *IEEE Trans. Power Syst.*, vol. 32, no. 5, pp. 3981–3991, Sep. 2017.

[14] D. Zhu, Z. Wang, Y. Ma, J. Hu, X. Zou, and Y. Kang, "Hybrid LVRT control of doubly-fed variable speed pumped storage to shorten crowbar operational duration," *IEEE Trans. Power Electron.*, vol. 39, no. 11, pp. 14192–14203, Nov. 2024.